THE JOURNAL OF PHYSICAL CHEMISTRY C

Article

pubs.acs.org/JPCC

Solution Combustion Synthesis, Characterization, and Photoelectrochemistry of $CuNb_2O_6$ and $ZnNb_2O_6$ Nanoparticles

A. Kormányos,[†,‡] A. Thomas,[§] M. N. Huda,[∥] P. Sarker,[∥] J. Ping Liu,[∥] N. Poudyal,[∥] C. Janáky,*[,†,‡] and K. Rajeshwar*[,§]

[†]MTA-SZTE, Lendület Photoelectrochemistry Research Group, Rerrich Square 1, Szeged H-6720, Hungary

[‡]Department of Physical Chemistry and Materials Science, University of Szeged, Rerrich Square 1, Szeged H-6720, Hungary

[§]Department of Chemistry and Biochemistry, University of Texas at Arlington, Arlington, Texas 76019, United States

[∥]Department of Physics, University of Texas at Arlington, Arlington, Texas 76019, United States

Supporting Information

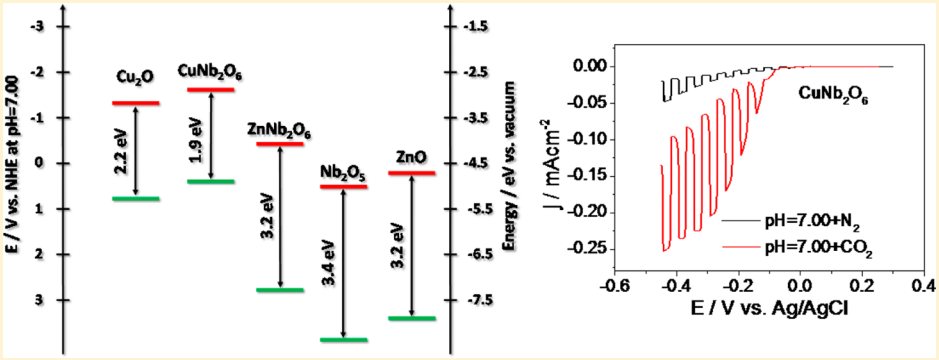

ABSTRACT: This study reports on the solution combustion synthesis of two different ternary niobium oxides, namely, *p*-$CuNb_2O_6$ and *n*-$ZnNb_2O_6$. Such ternary oxides are attractive candidates in the "Holy Grail" search for efficient and stable semiconductors for solar energy conversion and environmental remediation. We demonstrate how this time- and energy-efficient method is capable of synthesizing high surface area and crystalline nanoparticles of the above compounds with enhanced optoelectronic properties. The synthesized crystalline samples were characterized by powder X-ray diffraction (with Rietveld refinement for phase purity), diffuse reflectance UV−visible and Raman spectroscopy, electron microscopy, and photoelectrochemical (PEC) techniques. The band structure of these oxides was probed by linear sweep voltammetry and by measuring their photoaction spectra (internal photon to electron conversion efficiency vs wavelength). The obtained bandgap energy values (1.9 and 3.2 eV for the Cu- and Zn-containing compounds, respectively) were in reasonable agreement with those obtained via electronic structure calculations (2.07 and 3.53 eV). Finally, *p*-$CuNb_2O_6$ showed promising activity for the PEC reduction of CO_2, while *n*-$ZnNb_2O_6$ was active for sulfite and water photooxidation.

INTRODUCTION

One of the most critical challenges and paradigms of the 21st century is the shift in energy use from fossil fuels to renewable sources. Utilizing sunlight via solar fuels is unambiguously an effective strategy for attacking supply and environmental concerns.[1] While solar energy is the most abundant energy resource, the need for storage of the harvested energy is an unavoidable consequence of its intermittency. The generated electricity (e.g., by a photovoltaic cell) can be stored directly in batteries or used to produce solar fuels or other value-added chemicals. With this latter approach, the harnessed energy is stored in the form of chemical bonds. Photoelectrochemical (PEC) techniques can be used for this purpose, although many challenges have yet to be solved.[2−6] Currently, the two most important examples of solar fuels are H_2, obtained via water-splitting,[7] and high-energy chemicals, such as CO, CH_4, HCOOH, CH_3OH, etc., produced by the photochemical or PEC conversion of CO_2.[4,8,9]

The most extensively studied *n*-type metal oxide semiconductor is TiO_2, mostly because of its robustness, outstanding stability in aqueous media, coupled with nontoxicity and earth abundance of its constituent elements.[10,11] However, the wide bandgap (3.0−3.2 eV) of this material limits its application in solar energy utilization processes. A plethora of other *n*-type oxide semiconductors (binary or even ternary oxides) have been applied as photoanodes (e.g., ZnO, WO_3, Nb_2O_5, $SrTiO_3$).[12] On the other hand, *p*-type semiconductors

Special Issue: Kohei Uosaki Festschrift

Received: December 30, 2015
Revised: March 1, 2016

DOI: 10.1021/acs.jpcc.5b12738
J. Phys. Chem. C XXXX, XXX, XXX−XXX

can be used as photocathodes for driving various reductive processes such as H_2 evolution and CO_2 conversion. Copper-containing oxides are particularly relevant for these applications because of the rather unique capability of Cu-containing semiconductors to directly (i.e., without the use of any cocatalyst or redox mediator) photoelectroreduce CO_2. There are numerous examples in the literature highlighting the importance of copper oxides in photoelectrochemistry, including Cu_2O,[9,13] Cu_2O/CuO,[4,9] $CuFeO_2$,[14−16] $CuRhO_2$,[17] and $Cu_3Nb_2O_8$.[18]

A given photoelectrode material has to *simultaneously* meet certain requirements such as overlap of its optical absorption cross-section with the solar spectrum, optimal (conduction and valence) band edge positions to drive the required half-cell processes, good (chemical, electrochemical, or photoelectrochemical) corrosion resistance in aqueous media of variant pH, good charge transport, and interfacial electron transfer properties, and last but not least, cost-effectiveness and environmental compatibility of the selected material in terms of its earth abundance and toxicity, respectively.[19] Not surprisingly, no such "magic bullet" candidate has emerged yet, which fulfills all these requirements. Therefore, the drive to discover and develop new semiconductor materials, which might have all these properties, continues unabated.

In this search for new oxide photoelectrode materials, metal niobates are attractive candidates. One class of metal niobates conform to the formula MNb_2O_6, where M^{2+} = a + 2 cation (Zn, Cu, Co, Ni, Mn, etc.) with <1.0 Å ionic radius and an orthorhombic columbite structure.[20,21] To date, solid-state reactions at high temperatures have predominantly been the method of choice for synthesizing transition metal niobates as they are easily made from the corresponding metal oxide precursors.[17,22,23] However, the last two decades have witnessed a trend toward utilizing lower temperatures and a variety of *solution-based* techniques such as sol−gel synthesis, coprecipitation, or hydrothermal synthesis.[23−28] However, these approaches, along with their solid-state synthesis counterparts, suffer from a similar drawback: long reaction times (usually several hours) that prohibit the quick screening of large numbers of possible material candidates in combinatorial schemes. Furthermore, solid-state synthesis suffers from the need for high external energy input to maintain the elevated temperature during the synthesis. Hence, time- and energy-efficient synthetic routes for oxide semiconductors have particular relevance for solar fuel generation.

Solution combustion synthesis (SCS) is one such methodology. The most important features of this procedure[2,29−32] are (i) short reaction time, (ii) cost effectiveness, (iii) the lack of need for any special equipment, and most importantly, (iv) the ability to dope the host oxide by simple changes of the precursor fuel. Using carefully designed experimental conditions, the expulsion of various gases during the highly exothermic reaction also results in the formation of small-sized and high surface-area nanoparticles and nanostructures.[32] We and others have employed the SCS methodology for preparing simple oxides such as TiO_2,[33,34] ZnO,[35] WO_3,[36] as well as more complex oxides such as metal tungstates ($ZnWO_4$, $CuWO_4$, Ag_2WO_4, and $Ag_2BiW_2O_8$).[37,38]

This study demonstrates the use of SCS for preparing nanoparticles of two transition metal niobates: *p*-$CuNb_2O_6$ and *n*-$ZnNb_2O_6$. Particular focus was on the structural and morphological attributes, i.e., on generating high surface area and crystallinity of oxide products under time- and energy-efficient synthesis conditions. Additionally, PEC investigations of the above two semiconductors were carried out to evaluate their potential for solar fuel generation and for CO_2 reduction in particular. While *p*-$CuNb_2O_6$ showed activity for CO_2 photoreduction, *n*-$ZnNb_2O_6$ was active for sulfite and water photooxidation.

EXPERIMENTAL SECTION AND COMPUTATIONAL DETAILS

Materials. Copper nitrate hydrate, $Cu(NO_3)_2{\cdot}2.5\ H_2O$ (Alfa Aesar), zinc nitrate hexahydrate $Zn(NO_3)_2{\cdot}6H_2O$ (Alfa Aesar), and ammonium niobium oxalate monohydrate, $C_4H_4NNbO_9{\cdot}H_2O$ (Sigma-Aldrich), were used as the cation sources and oxidizers for the combustion reaction, and urea (Sigma-Aldrich) was used as the fuel. Commercially available samples of copper niobate and zinc niobate (Sigma-Aldrich) were used for benchmarking purposes. Na_2SO_4 (Alfa Aesar), Na_2SO_3 (Sigma-Aldrich), and $NaHCO_3$ (Reanal) were used in all the PEC experiments along with N_2 (Messer) and CO_2 (Messer) gases. All chemicals were of the highest purity commercially available and were used without further purification. Deionized water (MilliPore, 18 MΩ) was used to prepare all solutions.

Solution Combustion Synthesis. The respective metal and niobium precursor (see above) and urea (all in stoichiometric amounts, where the Cu^{2+} and Zn^{2+} concentration was 1.0 M) were dissolved in deionized water. Each solution was placed in individual crucibles and placed in a preheated furnace at 350 °C. The reaction occurred within 3−5 min. After combustion, the resultant products were removed, finely ground in a mortar/pestle, and subsequently annealed at 600 °C for 30 min. Once completed, the samples were washed, filtered, and dried in an air oven at 100 °C. [The effect of annealing at higher temperature (at 800 °C) was also investigated, but these samples showed a markedly inferior PEC behavior, presumably because of sintering.]

Electrode Preparation. The synthesized and annealed powder samples were spray-coated on Sn-doped indium oxide (ITO) glass electrode surface from a 10 mg mL^{-1} dispersion in isopropanol, which was sonicated for 30 min before use. The layers were sprayed consecutively on the ITO substrate (total surface area: 1 cm^2) by an Alder AD320 Airbrush spray gun (~2.5 mg cm^{-2} in the case of the copper niobate sample and ~5.0 mg cm^{-2} in the case of zinc niobate). The prepared thin films were heat-treated in an air oven at 350 °C for 2 h before use.

Physical Characterization. Thermogravimetric analysis/differential scanning calorimetry (TGA/DSC) on the precursor mixtures was carried out on a TA Instruments model Q600 instrument. The precursor mixtures were placed in an alumina crucible in air atmosphere with a flow rate of 100 mL min^{-1} at a heating rate of 10 °C min^{-1} up to 1000 °C. Powder X-ray diffraction (XRD) measurements were performed within the range of 2θ = 20−80° using a Rigaku Ultima IV instrument with Cu K_α source (λ = 1.5406 Å). Rietveld refinement was carried out using MDI Jade 8 software with initial model structures culled from the literature. Refinements were performed on each of the samples with reduced scale/background and full width at half-maximum (fwhm) parameters to account for all the peaks in the XRD patterns. The patterns were fit using a Gaussian profile function with displacement, allowing for any deviations from the model structure. The Scherrer equation was employed to determine the average

DOI: 10.1021/acs.jpcc.5b12738
J. Phys. Chem. C XXXX, XXX, XXX−XXX

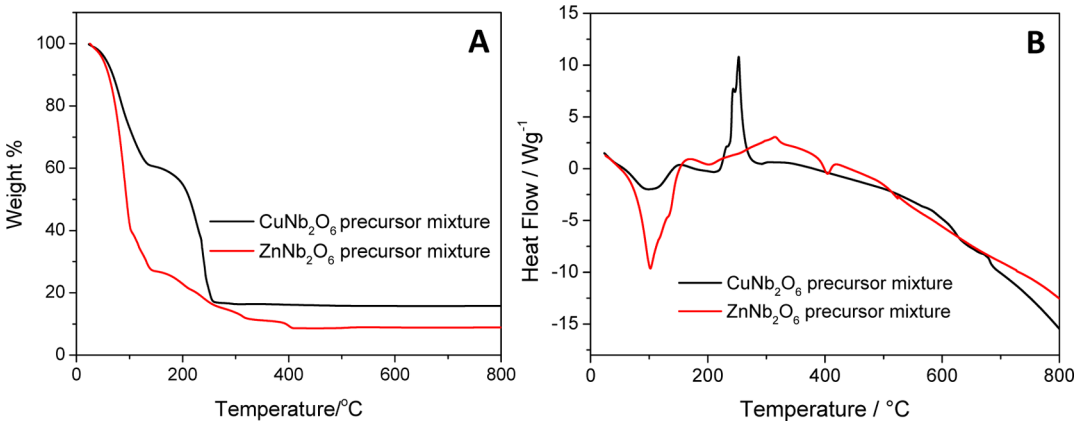

Figure 1. TGA (A) and DSC (B) profiles simulating SCS for copper niobate and zinc niobate.

crystallite size, using the two most intense diffractions in each case: [(131) and (102) for $CuNb_2O_6$, and (111) and (311) for $ZnNb_2O_6$].

Raman spectroscopy was performed on a DXR Raman microscope using a λ = 532 nm green laser. UV−visible diffuse reflectance spectra were collected on a PerkinElmer Lambda 35 spectrophotometer equipped with an integrating sphere. High-resolution transmission electron microscopy (HR−TEM) was performed on a Hitachi H9500 instrument at various magnifications. The synthesized and heat-treated powder samples were dispersed on carbon tape, while the thin films were used as-is. For scanning electron microscopy (SEM), a Hitachi S4700 FE-SEM instrument was used. For Brunauer−Emmett−Teller (BET) surface area measurements, a TriStar II 3020 instrument was used at a relative pressure range of P/P_0 = 0.05−0.3.

Photoelectrochemical (PEC) Characterization. All PEC measurements were performed on an Autolab PGSTAT10 instrument in a sealed two-compartment, quartz cell using a classical three-electrode setup. Platinum foil and Ag/AgCl (satd. NaCl) were used as counter- and reference electrodes, respectively. The electrolytes used were 0.1 M Na_2SO_4 (for both materials) or 0.1 M Na_2SO_3 (in the case of the zinc niobate samples) and 0.1 M $NaHCO_3$ (in the case of the copper niobate samples). For studies on the copper niobate samples, the solutions were saturated with N_2 and CO_2. The light sources were either a 100 W tungsten−halogen (Osram Xenophot HLX 64625 in an Oriel 60000 housing) or a 150 W tungsten−halogen (Fiberlite A 3000) lamp. The light source was placed 3 cm away from the working electrode surface in either case. The photovoltammograms were recorded under chopped illumination (0.1 or 0.05 Hz) and slow potential scan (1 or 2 mV s^{-1} sweep rate).

Incident photon-to-charge conversion efficiency (IPCE) measurements were performed on a Newport Quantum Efficiency Measurement System (QEPVSI-B) in a single-compartment, three-electrode quartz electrochemical cell. The wavelength range was 200−800 nm (with resolution, $\Delta\lambda$ = 10 or 20 nm and 3.16 mm slit width). The used solutions were: 0.1 M $NaHCO_3$ saturated with CO_2 in the case of the copper niobate samples and 0.1 M Na_2SO_3 in the case of the zinc niobate films.

Computational Details. The band structure calculations were performed within the framework of the standard frozen-core projector augmented-wave (PAW)[39,40] method using density functional theory (DFT) as implemented in the Vienna *ab initio* simulation package (VASP)[41,42] code. Exchange and correlation potentials were treated in the generalized gradient approximation as parametrized by Perdew−Burke−Ernzerhof (PBE).[43,44] Underestimation of electron localization is recognized as a major failure of both local and semilocal DFT calculations, in particular, for systems with localized d and f electrons.[45−47]

This failure manifests via the general trend of DFT to underestimate energy band gap values and to produce incorrect solutions for some 3d-based metal oxides. Thus, this shortcoming of DFT-GGA must be corrected in a computationally cost-effective manner. Therefore, DFT+U was used as a post-DFT correction method. In the present work, we used U_{eff} = 6 eV (U_{eff} = U − J = 7 − 1 = 6 eV, J = Stoner exchange parameter) to externally provide Coulomb correlation to both Cu 3d and Zn 3d orbitals in copper niobate and zinc niobate, respectively. The above value of U_{eff} was chosen from our previous work on Cu- and Zn-based compounds.[3,37,45,46,48,49]

The basis sets were expanded with plane waves with a kinetic energy cutoff of 400 eV. The ion positions and volumes were always relaxed without any symmetry constraint to allow the internal geometry and shape of the lattice to be changed freely until the force on each of the ions was 0.01 eV/Å or less.[50] The Brillouin zone integrations were performed using the second-order Methfessel−Paxton method.[51] For visualization of the crystal structures, VESTA (Visualization for Electronic and Structural Analysis)[52,53] was used.

All computations were performed using the High Performance Computing Facility at the University of Texas at Arlington and at the Texas Advanced Computing Center located in Austin, TX.

RESULTS AND DISCUSSION

Simulating the SCS Procedure by Thermal Analysis. A fundamental understanding of the SCS process can be gained by performing thermal analysis *during simulated synthesis*. Accordingly, thermogravimetric analysis (TGA) and differential scanning calorimetry (DSC) were employed to simulate the SCS process; TGA and DSC profiles simulating copper niobate and zinc niobate synthesis appear in Figures 1A and B, respectively. As seen in the TGA profile, two major mass losses occurred during the SCS process. The first one between 100 and ~ 170 °C is attributable to the elimination of water. The second mass loss, observed in a broad range between 170 and ~220 °C (for $CuNb_2O_6$) or 170 and ~400 °C (for $ZnNb_2O_6$), can be attributed to the combustion reaction and the

DOI: 10.1021/acs.jpcc.5b12738
J. Phys. Chem. C XXXX, XXX, XXX−XXX

subsequent combined decomposition of the metal salt precursor and fuel.

Both endothermic and exothermic peaks were observed on the DSC profiles (Figure 1B). A broad endothermic peak was witnessed at the initial stage of the process for both compounds. This feature is related to water loss from the precursor mixture and correlates with the first mass loss regime on the TGA curves (Figure 1A). An exothermic peak (at approximately 250 °C) for $CuNb_2O_6$ (Figure 1B) coincided with initiation of the combustion reaction accompanied by oxidation of the fuel and, ultimately, formation of the final oxide product. Note that the mass remains the same at temperatures higher than ∼250 °C (for $CuNb_2O_6$) and ∼400 °C (for $ZnNb_2O_6$) (Figure 1A). The corresponding exothermic feature for $ZnNb_2O_6$ is much weaker and appears at ∼300 °C (Figure 1B). The baseline slope change in the DSC at higher temperatures (past ∼400 °C), which is not accompanied by any corresponding TGA features, may be attributed to gradual changes in the heat capacity of both materials.

Structural and Morphological Characterization. Copper niobate ($CuNb_2O_6$) exhibits two polymorphs: monoclinic ($P2/c$) and an orthorhombic form.[20,54] A literature survey reveals the formation of these two $CuNb_2O_6$ polymorphs at different reaction temperatures; i.e., the monoclinic polymorph can be obtained at temperatures <740 °C, while the orthorhombic form is formed at temperatures >740 °C.[54−56] Zinc niobate ($ZnNb_2O_6$) commonly crystallizes in an orthorhombic structure with space group *Pbcn*/*Pnab*.[20]

In the $CuNb_2O_6$ and $ZnNb_2O_6$ structure, the Cu:Nb and Zn:Nb atom centers are each surrounded by six oxygen atoms which form zigzag chains of CuO_6:NbO_6 and ZnO_6:NbO_6 Jahn−Teller distorted octahedra connected by edge-sharing. These zigzag chains in turn are connected by corner sharing, creating an ordered repeating M−MO_6−MO_6−M−MO_6−MO_6−M octahedral layer, where M = CuO_6 or ZnO_6 in $CuNb_2O_6$ and $ZnNb_2O_6$, respectively.[20,21] See Figures 2A and B for model structure representations of the two metal niobates.

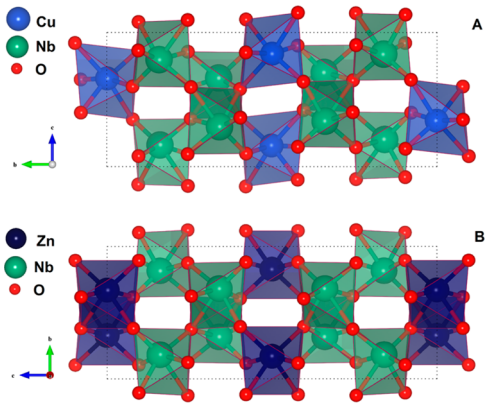

Figure 2. Polyhedral models of the crystal structures for (A) $CuNb_2O_6$ and (B) $ZnNb_2O_6$.

For both these compounds, studies oriented toward the tuning of bandgap energies (or "band engineering") have served to open up further avenues for heterogeneous photocatalysis and PEC applications.[17,55−60]

The as-synthesized, annealed, and respective commercial samples were characterized by powder X-ray diffraction (XRD) with subsequent Rietveld refinement. Each of the combustion-synthesized samples was annealed at 600 °C to enhance the degree of crystallinity, as well as to eliminate any possible impurity or carbon residue from SCS. [However, it was worth noting that even without heat treatment fairly crystalline products were observed for both SCS samples; see Table 1 below.] Figures 3A and B illustrate XRD patterns for copper niobate and zinc niobate, respectively.

Table 1. Calculated Average Crystallite Size and Surface Area of the SCS-Derived Niobate Samples

semiconductor material		crystallite size (nm)	surface area ($m^2\ g^{-1}$)
$CuNb_2O_6$	as-synthesized	8.3 ± 1	16.0
	annealed at 600 °C	20.3 ± 2	8.8
	commercial	19.0 ± 3	<5
$ZnNb_2O_6$	as-synthesized	4.1 ± 2	64.9
	annealed at 600 °C	15.8 ± 3	18.4
	commercial	31.7 ± 3	<5

The XRD pattern of copper niobate, before and after heat treatment, clearly yielded a material more crystalline in nature than the zinc counterpart. This trend was in accordance with the high exothermicity of the reaction as noted in the DSC data (Figure 1B). Rietveld analysis of the annealed sample yielded a single-phase monoclinic $CuNb_2O_6$ structure (see Figure S1) in agreement with the 83-0369 JCPDS file and with other data from the literature.[22,54,62] Formation of the monoclinic polymorph is also consistent with the expectation from earlier studies[52,53] that shows the proclivity of this form to be dominant at "low" synthesis temperatures (see above).

We carefully examined the XRD patterns for other possible copper niobates (e.g., $CuNbO_3$, $Cu_3Nb_2O_8$, etc.); their presence in the SCS samples can be excluded. This trend is further corroborated by an earlier report on coprecipitation of $CuNb_2O_6$, which demonstrated that the monoclinic structure was preferred if the oxalate precursor was used in the preparation.[55] Finally, we note that although good crystallinity was displayed by the commercial $CuNb_2O_6$ sample a multiphase structure was indicated by Rietveld refinement in this case, with the secondary phase (amounting to ∼35% by mass) being Nb_2O_5.

Rietveld refinement of the annealed zinc niobate sample yielded a multiphase structure comprised of an orthorhombic $ZnNb_2O_6$ (dominant) and ZnO (secondary) phase (Figure S1B), each matching with JCPDS files 76-1827 and 89-0511, respectively, and with other data from the literature.[63] The ZnO phase (accounting for ∼25% of the sample) perhaps was generated from incomplete reaction of the decomposed zinc nitrate and the other precursors and then being calcined by the exothermic reaction's internal temperature and subsequent anneal. The commercial benchmark sample, however, was single phase exhibiting high crystallinity as illustrated in Figure 3B.

The most intense peaks were used to calculate the average crystallite sizes for both materials. As displayed in Table 1, there was a clear (and expected) trend that particle size increased with thermal anneal. In accordance, BET analysis in turn showed a decrease in the surface area for each of the samples. This tendency can be attributed to fusing of individual nanoparticles (i.e., sintering) upon calcination. The strikingly

DOI: 10.1021/acs.jpcc.5b12738
J. Phys. Chem. C XXXX, XXX, XXX−XXX

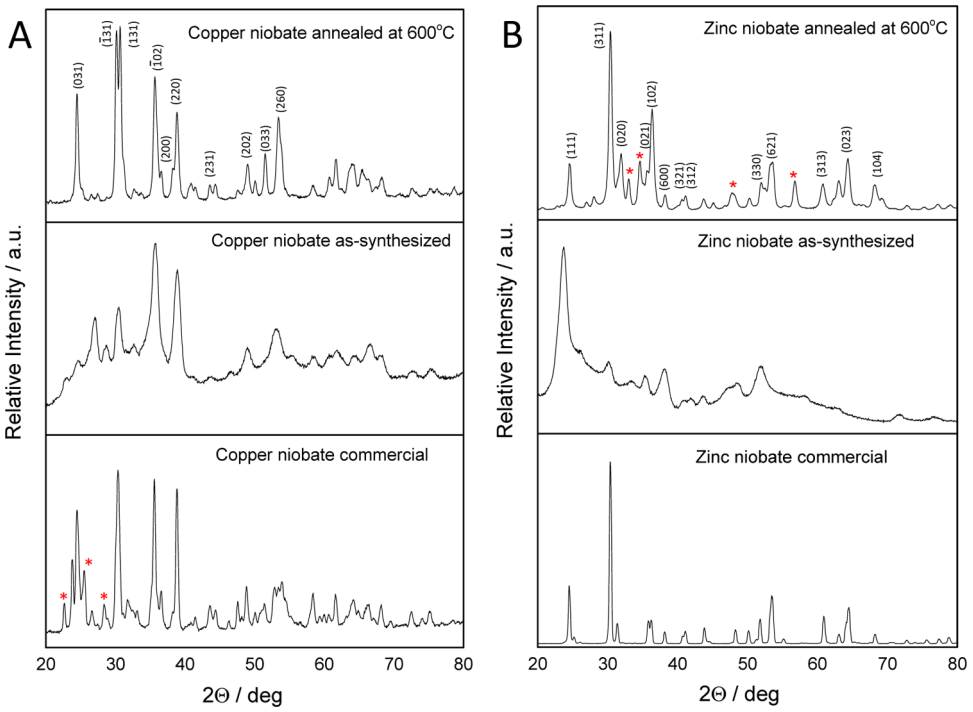

Figure 3. XRD patterns for (A) $CuNb_2O_6$ and (B) $ZnNb_2O_6$ samples; (*) represents the presence of ZnO and Nb_2O_5 in $ZnNb_2O_6$ and $CuNb_2O_6$, respectively.

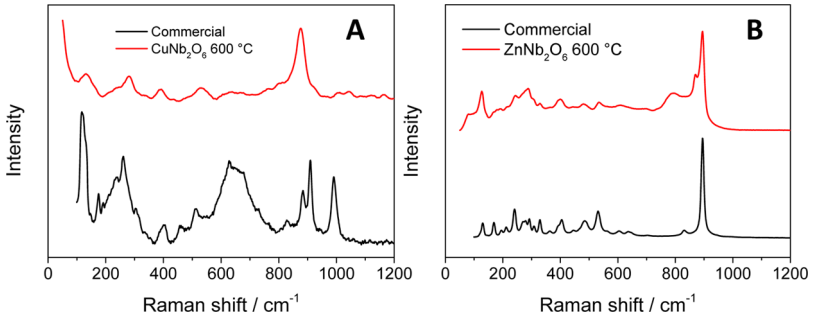

Figure 4. Comparison of Raman spectra for commercial and annealed samples: (A) $CuNb_2O_6$ and (B) $ZnNb_2O_6$.

small surface area of the commercial $ZnNb_2O_6$ sample (and $CuNb_2O_6$, for that matter) is worthy of note.

There are no Raman data in the literature for $CuNb_2O_6$ (at least to our knowledge); however, comparison of the SCS sample with its commercial counterpart (Figure 4A) furnished important insights. Most importantly, beyond the bands common to both samples, there were important differences: the two broad bands, centered at 660 and 261 cm^{-1}, and the two well-defined, narrow peaks at 992 and 116 cm^{-1} of the commercial sample corresponded to the Nb_2O_5 impurity,[64,65] in agreement with the trend in the XRD data presented earlier.

Figure 4B shows a comparison of the Raman spectra of the commercial and the heat-treated $ZnNb_2O_6$ samples. The two sets of spectra exhibited many identical vibrations. According to literature data, four major peaks can be assigned as A_g modes (894 and 292 cm^{-1}) and as B_{2g} modes (329 and 210 cm^{-1}).[63] Differences in the two sets of spectra in Figure 4B (e.g., pronounced shoulder in the 894 cm^{-1} band for the SCS sample) are attributable to the ZnO minority phase in the SCS sample.

The morphological attributes of the oxide samples were gleaned from electron microscopy (both SEM and TEM). Figure 5 shows SEM images of spray-coated and heat-treated copper niobate (A, B) and zinc niobate (C, D) thin films. There was no significant difference between the as-is and annealed samples; the thin films possessed similar morphology. Further, the electrode surfaces were coated evenly in both cases (unlike for the samples annealed at 800 °C, where no coherent layer was obtained).

The TEM images in Figures 6A and B for the $CuNb_2O_6$ and $ZnNb_2O_6$ nanoparticles, respectively, revealed a slightly bigger particle size (typically 20−60 nm) compared to the XRD data. The particles were also aggregated. Closer inspection of the particles via HR-TEM revealed visible lattice fringes for both materials. Interplanar spacings for the $CuNb_2O_6$ sample (Figure 6C), 0.276, 0.292, and 0.714 nm, corresponding to the (202), (310), and (200) lattice planes, may be discerned; these are in good agreement with data in prior studies for samples derived from other synthesis methods.[23,54] For the $ZnNb_2O_6$ sample (Figure 6D) these values were 0.272, 0.291, and 0.361 nm, corresponding to the (002), (020), and (400) lattice planes, respectively. These HR-TEM data are also consistent with values in earlier reports,[63,66] as well as with the XRD data presented earlier.

DOI: 10.1021/acs.jpcc.5b12738
J. Phys. Chem. C XXXX, XXX, XXX−XXX

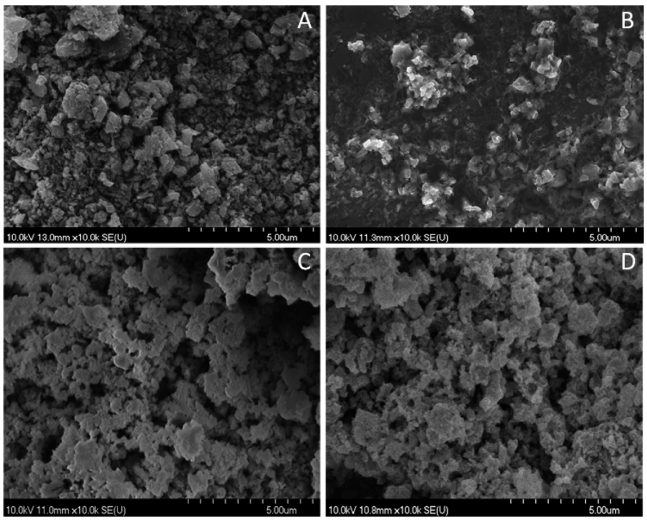

Figure 5. SEM images of (A) $CuNb_2O_6$ as-is and (B) $CuNb_2O_6$ annealed at 600 °C and (C) $ZnNb_2O_6$ as-is and (D) $ZnNb_2O_6$ annealed at 600 °C. The samples in all cases were spray-coated and heat-treated thin films on ITO substrate.

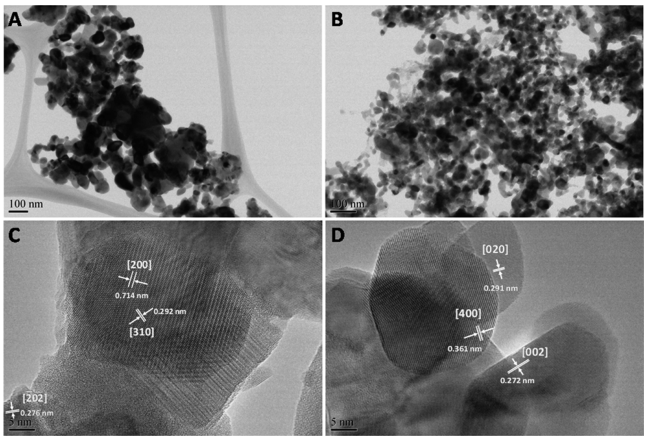

Figure 6. TEM images of (A) $CuNb_2O_6$ and (B) $ZnNb_2O_6$ annealed at 600 °C and (C), (D) corresponding high-resolution images displaying the presence of lattice fringes.

Optical Properties. UV−vis diffuse reflectance spectroscopy was employed to estimate the bandgap energy values of the synthesized oxides. This was achieved by generating Tauc plots, namely, a plot of the Kubelka−Munk function versus photon energy ($\alpha h\nu^n$ vs $h\nu$).[67,68,69] Figure 7 contains representative plots for $CuNb_2O_6$ (Figure 7A) and $ZnNb_2O_6$ (Figure 7B), respectively. Table 2 displays the experimental, calculated, and literature energy bandgap values. The $CuNb_2O_6$ samples showed an indirect bandgap of 1.77 eV, again falling within the range reported in the literature. For $ZnNb_2O_6$, an indirect bandgap of 3.55 eV was obtained. This value was within the range of previously reported studies of $ZnNb_2O_6$ as shown in Table 2. The optical data in Figure 7B also clearly show the presence of the ZnO minority phase in the SCS sample. Thermal anneal, as expected, did not significantly perturb the values of the bandgap energy for either $CuNb_2O_6$ or $ZnNb_2O_6$ (Table 2).

Table 2. Optical Properties of the Solution Combustion-Synthesized Metal Niobate Samples

Sample	Visual Appearance	Bandgap energy (eV)			
		As-synthesized	Annealed at 600 °C	Calculated values	Reported values
$CuNb_2O_6$	Dark brown 	1.72 ± 0.02	1.77 ± 0.01	2.07	1.45 – 2.5[6,17,59]
$ZnNb_2O_6$	White 	3.25 ± 0.02	3.55 ± 0.05	3.53	3.31 – 4.06[26,68,69]

Electronic Band Structure Calculations. Electronic band structures were calculated for the two oxides along the special symmetry points in the Brillouin zone. The DFT + U electronic band structures of $CuNb_2O_6$ and $ZnNb_2O_6$ are shown in Figures 8A and B, respectively. $CuNb_2O_6$ had a net magnetic moment of 4.00 μ_B, thereby having different spin-up and spin-down contributions. The major difference in $CuNb_2O_6$ band structures in the two spin directions was the presence of partially occupied intermediate bands in the spin-down channel near the Fermi level as shown in Figure 8A. The presence of intermediate bands split the bandgap of $CuNb_2O_6$ into two sub-bandgaps: one was direct at Γ with a value of 0.92 eV, and the other one was indirect with a value of 2.07 eV along the Γ → C region. These partially occupied bands near the Fermi level can presumably contribute to the p-type conductivity of $CuNb_2O_6$. However, the bands (especially VB) are relatively flat. As a result, despite their intrinsic presence, holes may not be very mobile, and hence the conductivity due to holes may not be significant.

Figure 8B exhibits an indirect bandgap of 3.53 eV for $ZnNb_2O_6$ (very close to the experimental optical absorption value) occurring along Γ → X. The CB and the VB are mostly dispersive, indicating lower effective masses of holes and higher effective masses of electrons, respectively. Unlike the copper counterpart, $ZnNb_2O_6$ had a net magnetic moment of 0 μ_B.

Photoelectrochemical (PEC) Characterization. Figure 9A shows the comparison of linear sweep photovoltammetry data for $CuNb_2O_6$ in various aqueous solutions, while the sample was illuminated by visible light. First, the photovoltammograms were recorded in 0.1 M Na_2SO_4 saturated with N_2 (black curve) to map the general PEC behavior of the sample. Note that PEC activity manifests as cathodic photocurrent flow diagnosing that the minority carriers are electrons. Accordingly, based on these measurements, the $CuNb_2O_6$ sample has p-type semiconductor characteristics in good agreement with theoretical predictions (see above).

Literature reports[6,18,59−61] suggest that the band edge positions of copper niobates are in a regime that would make these materials photoelectroactive toward the reduction of CO_2. Accordingly, the PEC performance of the p-$CuNb_2O_6$ sample was tested in CO_2- and N_2-saturated 0.1 M $NaHCO_3$ solution (red and blue curves, Figure 9A). Two major observations can be made: (a) The photocurrents are two times higher (at E = −0.4 V) if the solution is saturated with CO_2. (b) In the presence of HCO_3^-, PEC CO_2 reduction still occurs even if the solution is saturated with N_2.

To exclude the effect of pH and the possibility that the higher photocurrent is simply a result of enhanced proton reduction occurring because of the more acidic pH (induced by CO_2), the photovoltammograms, which were rerecorded in CO_2-saturated $NaHCO_3$ solution, can be compared with the one measured in 0.1 M Na_2SO_4. This comparison clearly

DOI: 10.1021/acs.jpcc.5b12738
J. Phys. Chem. C XXXX, XXX, XXX−XXX

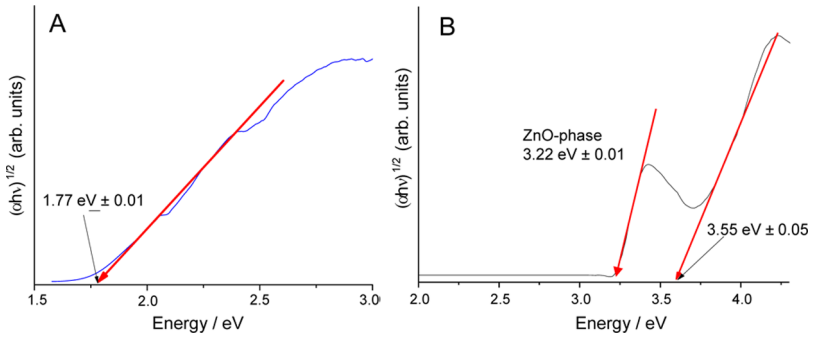

Figure 7. Tauc plots of (A) $CuNb_2O_6$ and (B) $ZnNb_2O_6$ (with a minority ZnO phase) annealed at 600 °C.

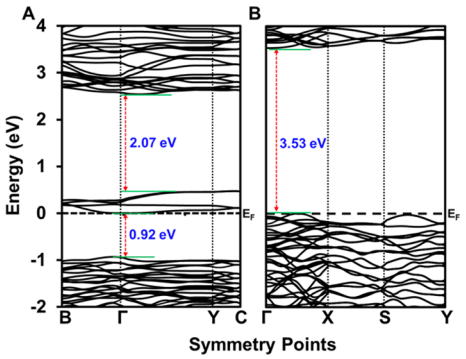

Figure 8. Electronic band structures of (A) $CuNb_2O_6$ and (B) $ZnNb_2O_6$.

confirms the notion that pH has a negligible effect on the magnitude of the photocurrents. The dramatic increase in the presence of CO_2 (i.e., 6 times higher photocurrents at $E = -0.4$ V) is clearly attributable to the ability of $CuNb_2O_6$ to photoelectrochemically reduce CO_2. At this point we note that, as far as we know, there is only one prior report[18] in the literature on the PEC reduction of CO_2 on a copper niobate ($Cu_3Nb_2O_8$) photocathode, and our SCS material shows comparable photoactivity. It is worth noting that the copper niobate photocathode in this prior study was prepared by a different method, viz., spin-coating of a sample derived from metal organic decoposition.[18]

The onset potential of photocurrent flow at semiconductor/electrolyte interfaces is approximately related to the flat-band potential if appreciable shifts induced by carrier trapping at the interface can be neglected.[70] Thus, from the data in Figure 9A, the position of the valence band (VB) edge in *p*-$CuNb_2O_6$ can be estimated to be 0.170 V vs Ag/AgCl.

Figure 9B contains representative photocurrent/potential data for a $ZnNb_2O_6$ thin film electrode recorded in 0.1 M Na_2SO_4 (black curve) and in 0.1 M Na_2SO_3 (red curve) under chopped UV-light irradiation. These PEC experiments revealed that $ZnNb_2O_6$ behaved as a typical *n*-type semiconductor. However, only moderate photocurrents were measured in the Na_2SO_4 solution. To further evaluate the PEC behavior, a hole scavenger (0.1 M Na_2SO_3) was employed, and linear sweep photovoltammograms were re-recorded. The maximum photocurrent was approximately one magnitude higher (0.2 mA cm^{-2} at 0.25 V) compared to the one recorded in Na_2SO_4. Two separate processes were observed on this curve: (a) SO_3^{2-} oxidation up to $E = -0.2$ V and (b) SO_3^{2-} and water oxidation above −0.2 V. As in the *p*-$CuNb_2O_6$ case but now for an *n*-type semiconductor, the onset potential of this voltammogram can again be related to the Fermi level of the *n*-$ZnNb_2O_6$ sample. Thus, the position of the *conduction band* (CB) edge can be estimated (−0.78 V vs Ag/AgCl). We note here that the presence of the ZnO minority phase may also contribute to the measured photocurrents either directly (ZnO is also an *n*-type semiconductor) or indirectly, via the so-called mixed crystal effect, by ensuring better charge separation.[71]

Finally, it is worth noting that linear sweep photovoltammograms were also recorded for the respective commercial samples (Figure S2). The most important conclusions to be drawn from these comparative studies are that (i) the character of the curves is similar to those recorded for the SCS samples and (ii) the SCS samples massively outperform their commercial counterparts in the case of both oxides, in terms

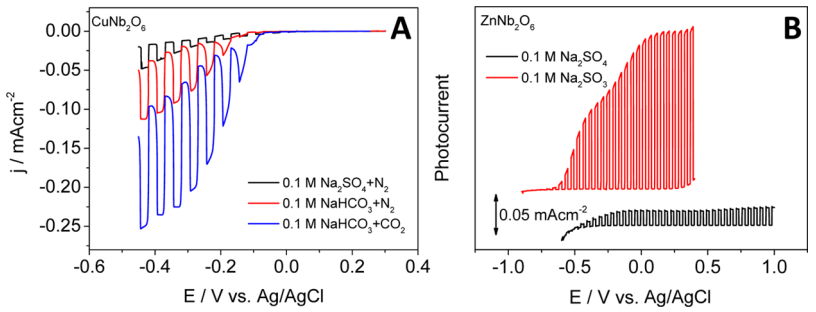

Figure 9. (A) Comparison of PEC activity of the $CuNb_2O_6$ sample in various solutions: in 0.1 M Na_2SO_4 saturated with N_2, pH = 7.00 (black curve); in 0.1 M $NaHCO_3$ saturated with N_2, pH ∼ 9.00 (red curve); and in 0.1 M $NaHCO_3$ saturated with CO_2, pH ∼ 7.00 (blue curve); applying a sweep rate of 1 mV s^{-1}, using a 150 W tungsten−halogen visible lamp. (B) Photovoltammogram of the $ZnNb_2O_6$ sample recorded in 0.1 M Na_2SO_4 and in 0.1 M Na_2SO_3 applying a sweep rate of 2 mV s^{-1}, using a 100 W tungsten−halogen UV lamp.

DOI: 10.1021/acs.jpcc.5b12738
J. Phys. Chem. C XXXX, XXX, XXX−XXX

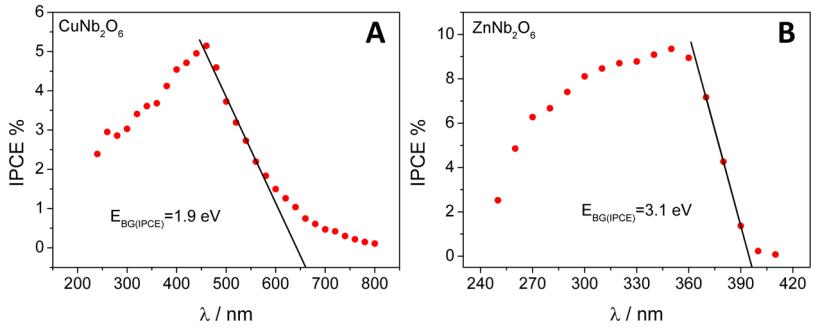

Figure 10. Photoaction spectra for the $CuNb_2O_6$ sample in 0.1 M $NaHCO_3$ saturated with CO_2 at $E = -0.35$ V and $\Delta\lambda = 20$ nm (A) and $ZnNb_2O_6$ sample registered in 0.1 M Na_2SO_3 at $E = 0.1$ V and $\Delta\lambda = 10$ nm (B).

of the measured photocurrents. In other words, there is an order of magnitude difference in the photocurrents.

Figure 10 contains photoaction spectra for *p*-$CuNb_2O_6$ (Figure 10A) and *n*-$ZnNb_2O_6$ (Figure 10B), respectively. The *p*-$CuNb_2O_6$ sample was photoactive in a broad wavelength range. Although the IPCE curve (Figure 10A) suggests that the *p*-$CuNb_2O_6$ sample can utilize UV-light, our experiments showed an increased rate of photocorrosion when the sample was illuminated by UV-light (data not presented). The curve had a maximum at 460 nm (5.2%), and the decrease of the efficiency was not as sharp as in the case of the *n*-$ZnNb_2O_6$ sample (Figure 10B); at wavelengths higher than 800 nm, the photoactivity diminished. The bandgap energy ($E_{BG(IPCE)}$ = 1.9 eV) was estimated by fitting the cutoff region with a straight line segment and extrapolating to the wavelength axis. This value roughly matches with our optical data and the results of the DFT calculations presented earlier.

Figure 10B shows the photoaction spectrum (IPCE data) registered at $E = 0.1$ V in 0.1 M Na_2SO_3. It can be concluded that *n*-$ZnNb_2O_6$ is photoelectroactive only when illuminated by UV-light, a conclusion well supported by the optical and PEC data presented earlier. The IPCE curve reached its maximum at 350 nm (9.4%) (Figure 10B) followed by a sharp cutoff. By fitting a linear segment on this part of the curve, the bandgap energy can be estimated ($E_{BG(IPCE)}$ = 3.1 eV), again in reasonable agreement with the data from the UV−vis measurements and DFT calculations.

Stability tests were performed using repetitive cycles of linear sweep voltammetry; the corresponding data are contained in Figure S3. $ZnNb_2O_6$ showed impressive PEC stability, as deduced from the perfect overlap of the series of subsequently recorded photovoltammograms (Figure S3B). As for $CuNb_2O_6$, it exhibited the instability often reported for copper-containing *p*-type semiconductors. There was a notable decrease in the photocurrent during subsequent cycles, especially when the electrode was polarized at negative potentials (Figure S3A). This effect also manifested in the continuous decay in the photocurrent during long-term measurements, similar to what was observed for another copper niobate ($Cu_3Nb_2O_8$) earlier (see ref 18).

Finally, the bandgap energy values derived earlier along with the data on band edge positions as inferred from the PEC measurements and afforded mapping of the energy band diagrams for both compounds on a common scale; this is shown in Figure 11. Also compared are the corresponding data for the three parent oxides, Cu_2O, ZnO, and Nb_2O_5, respectively. Relative to the parent (binary) oxides, the ternary oxides have higher CB positions, translating in turn to higher

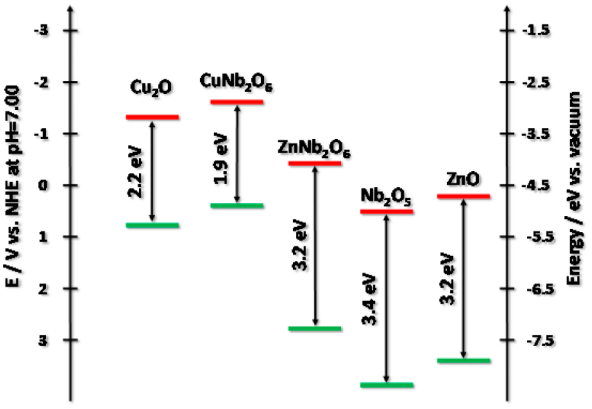

Figure 11. Energy band diagrams (determined from PEC measurements) for $ZnNb_2O_6$ and $CuNb_2O_6$, compared to the respective monometallic (binary) oxides. The latter were constructed from data in ref 72.

reducing power for the photogenerated electrons in these compounds. This is a useful attribute in the use of these compounds for driving photoreduction processes such as CO_2 splitting.

CONCLUSIONS

In this study, the feasibility of solution combustion synthesis (SCS) of *p*-$CuNb_2O_6$ and *n*-$ZnNb_2O_6$ nanoparticles was demonstrated. As a result of the highly exothermic conditions prevailing in SCS, both oxides were at least partly crystalline even without additional thermal anneal. The surface areas of these nanoparticles also far exceeded those of commercial benchmark samples. This is a significant finding underlining the utility of SCS for generating nanoparticles for any catalytically relevant application where this parameter plays a key role. Photoelectrochemical measurements established that $CuNb_2O_6$ is a *p*-type semiconductor with a bandgap energy of ∼1.9 eV. On the other hand, $ZnNb_2O_6$ exhibited *n*-type behavior with a bandgap of ∼3.1 eV.

Other than differences in the type of semiconductor electronic conductivity and bandgap energy values for the two metal niobates, band structure calculations also revealed important differences with an intermediate band being identified for the Cu compound. Finally *p*-$CuNb_2O_6$ showed promising activity toward the photoelectrochemical reduction of CO_2 even without any cocatalyst. This attribute appears to be a common denominator for *p*-type copper oxide semiconductors as also gleaned from our companion studies on copper oxides.[4,9,73,74] On the other hand, *n*-$ZnNb_2O_6$ exhibited

DOI: 10.1021/acs.jpcc.5b12738
J. Phys. Chem. C XXXX, XXX, XXX−XXX

photoactivity for the oxidation of sulfite (an environmental pollutant) and water (a source of solar fuel).

Taken as a whole, the data presented above build upon the corpus of earlier studies from our laboratories[2,33−35] and by other research groups,[29−35,72] demonstrating the versatility of SCS for preparing a variety of oxide semiconductor nanoparticles for solar fuel generation and environmental remediation.

■ ASSOCIATED CONTENT

Supporting Information

The Supporting Information is available free of charge on the ACS Publications website at DOI: 10.1021/acs.jpcc.5b12738.

Additional XRD (Rietveld refinement) and PEC results (PDF)

■ AUTHOR INFORMATION

Corresponding Authors

*E-mail: janaky@chem.u-szeged.hu (C. Janáky).
*E-mail: rajeshwar@uta.edu (K. Rajeshwar).

Notes

The authors declare no competing financial interest.

■ ACKNOWLEDGMENTS

K.R. thanks the National Science Foundation (CHE-1303803) and Sid Richardson Carbon & Energy Co. (Fort Worth, TX) for partial support of this research. C.J. gratefully acknowledges the support from the Hungarian Academy of Science, through its "Momentum" Excellence Program (LP2014-3). Work by MNH was partially supported by the National Science Foundation (CBET-1133672). For computational facilities, the High Performance Computing Center at the University of Texas at Arlington (UTA) and Texas Advanced Computing Center at Austin, TX, are acknowledged. Many of the characterization techniques (e.g., SEM, HR-TEM) used facilities at the Characterization Center for Materials & Biology at UTA. Finally, JPL thanks the Army Research Office, Grant No.W911NF-11-1-0507. We thank the three anonymous reviewers for their constructive criticisms of earlier versions of this manuscript.

■ REFERENCES

(1) Tran, P. D.; Wong, L. H.; Barber, J.; Loo, J. S. C. Recent Advances in Hybrid Photocatalysts for Solar Fuel Production. *Energy Environ. Sci.* **2012**, *5*, 5902−5918.

(2) Rajeshwar, K.; de Tacconi, N. R. Solution Combustion Synthesis of Oxide Semiconductors for Solar Energy Conversion and Environmental Remediation. *Chem. Soc. Rev.* **2009**, *38*, 1984−1998.

(3) Prasher, D.; Chong, M.; Chang, Y.; Sarker, P.; Huda, M. N.; Gaillard, N. Development of Metal Tungstate Alloys for Photoelectrochemical Water Splitting. *Proc. SPIE* **2013**, *8822*, 88220E1−88220E7.

(4) Ghadimkhani, G.; de Tacconi, N. R.; Chanmanee, W.; Janaky, C.; Rajeshwar, K. Efficient Solar Photoelectrosynthesis of Methanol from Carbon Dioxide Using Hybrid CuO-Cu_2O Semiconductor Nanorod Arrays. *Chem. Commun.* **2013**, *49*, 1297−1299.

(5) Sivula, K. Metal Oxide Photoelectrodes for Solar Fuel Production, Surface Traps, and Catalysis. *J. Phys. Chem. Lett.* **2013**, *4*, 1624−1633.

(6) Joshi, U. A.; Palasyuk, A.; Arney, D.; Maggard, P. A. Semiconducting Oxides to Facilitate the Conversion of Solar Energy to Chemical Fuels. *J. Phys. Chem. Lett.* **2010**, *1*, 2719−2726.

(7) Paracchino, A.; Laporte, V.; Sivula, K.; Grätzel, M.; Thimsen, E. Highly Active Oxide Photocathode for Photoelectrochemical Water Reduction. *Nat. Mater.* **2011**, *10*, 456−461.

(8) Inoue, T.; Fujishima, A.; Konishi, S.; Honda, K. Photoelectrocatalytic Reduction of Carbon Dioxide in Aqueous Suspensions of Semiconductor Powders. *Nature* **1979**, *277*, 637−638.

(9) Rajeshwar, K.; de Tacconi, N. R.; Ghadimkhani, G.; Chanmanee, W.; Janáky, C. Tailoring Copper Oxide Semiconductor Nanorod Arrays for Photoelectrochemical Reduction of Carbon Dioxide to Methanol. *ChemPhysChem* **2013**, *14*, 2251−2259.

(10) Fujishima, A.; Honda, K. Electrochemical Photolysis of Water at a Semiconductor Electrode. *Nature* **1972**, *238*, 37−38.

(11) Linsebigler, A.; Lu, G.; Yates, J. Photocatalysis on TiO_2 Surfaces: Principles, Mechanisms, and Selected Results. *Chem. Rev.* **1995**, *95*, 735−758.

(12) Rajeshwar, K. Solar Energy Conversion and Environmental Remediation Using Inorganic Semiconductor/Liquid Interfaces: The Road Traveled and the Way Forward. *J. Phys. Chem. Lett.* **2011**, *2*, 1301−1309.

(13) Li, C.; Li, Y.; Delaunay, J. A Novel Method to Synthesize Highly Photoactive Cu_2O Microcrystalline Films for Use in Photoelectrochemical Cells. *ACS Appl. Mater. Interfaces* **2014**, *6*, 480−486.

(14) Kang, U.; Choi, S. K.; Ham, D. J.; Ji, S. M.; Choi, W.; Han, D. S.; Abdel-Wahab, A.; Park, H. Photosynthesis of Formate from CO_2 and Water at 1% Energy Efficiency via Copper Iron Oxide Catalysis. *Energy Environ. Sci.* **2015**, *8*, 2638−2643.

(15) Gu, J.; Wuttig, A.; Krizan, J. W.; Hu, Y.; Detweiler, Z. M.; Cava, R. J.; Bocarsly, A. B. Mg-Doped $CuFeO_2$ Photocathodes for Photoelectrochemical Reduction of Carbon Dioxide. *J. Phys. Chem. C* **2013**, *117*, 12415−12422.

(16) Prévot, M. S.; Guijarro, N.; Sivula, K. Enhancing the Performance of a Robust Sol-Gel-Processed p-Type Delafossite $CuFeO_2$ Photocathode for Solar Water Reduction. *ChemSusChem* **2015**, *8*, 1359−1367.

(17) Gu, J.; Yan, Y.; Krizan, J. W.; Gibson, Q. D.; Detweiler, Z. M.; Cava, R. J.; Bocarsly, A. B. p-Type $CuRhO_2$ as a Self-Healing Photoelectrode for Water Reduction under Visible Light. *J. Am. Chem. Soc.* **2014**, *136*, 830−833.

(18) Kamimura, S.; Murakami, N.; Tsubota, T.; Ohno, T. Fabrication and Characterization of a p-Type $Cu_3Nb_2O_8$ Photocathode toward Photoelectrochemical Reduction of Carbon Dioxide. *Appl. Catal., B* **2015**, *174−175*, 471−476.

(19) Rajeshwar, K.; Thomas, A.; Janáky, C. Photocatalytic Activity of Inorganic Semiconductor Surfaces: Myths, Hype, and Reality. *J. Phys. Chem. Lett.* **2015**, *6*, 139−147.

(20) Pullar, R. C. The Synthesis, Properties, and Applications of Columbite Niobates ($M^{2+}Nb_2O_6$): A Critical Review. *J. Am. Ceram. Soc.* **2009**, *92*, 563−577.

(21) Norwig, J.; Weitzel, H.; Paulus, H.; Lautenschläger, G.; Rodriguez-Carvajal, J.; Fuess, H. Structural Relations in Mixed Oxides $Cu_xZn_{1-x}Nb_2O_6$. *J. Solid State Chem.* **1995**, *115*, 476−483.

(22) Pullar, R. C.; Lai, C.; Azough, F.; Freer, R.; Alford, N. M. Novel Microwave Dielectric LTCCs Based upon V_2O_5 Doped $M^{2+}Cu_2Nb_2O_8$ Compounds (M^{2+} = Zn, Co, Ni, Mg and Ca). *J. Eur. Ceram. Soc.* **2006**, *26*, 1943−1946.

(23) Sato, M.; Hama, Y. Lithium Insertion Characteristics of $CuNb_2O_6$. *J. Solid State Chem.* **1995**, *118*, 193−198.

(24) Ngamjarurojana, A.; Khamman, O.; Yimnirun, R.; Ananta, S. Effect of Calcination Conditions on Phase Formation and Particle Size of Zinc Niobate Powders Synthesized by Solid-State Reaction. *Mater. Lett.* **2006**, *60*, 2867−2872.

(25) Zhang, Y. C.; Fu, B.; Liu, Q. Preparation of $CuNb_2O_6$ Nanocrystalline Powders by Sol−gel Method. *J. Alloys Compd.* **2009**, *477*, 716−719.

(26) Hsiao, Y. J.; Fang, T. H.; Ji, L. W. Synthesis and Luminescent Properties of $ZnNb_2O_6$ Nanocrystals for Solar Cell. *Mater. Lett.* **2010**, *64*, 2563−2565.

DOI: 10.1021/acs.jpcc.5b12738
J. Phys. Chem. C XXXX, XXX, XXX−XXX

(27) Dai, J.; Zhang, C.; Shi, L.; Song, W.; Wu, P.; Huang, X. Low-Temperature Synthesis of $ZnNb_2O_6$ Powders via Hydrothermal Method. *Ceram. Int.* **2012**, *38*, 1211−1214.
(28) Deshpande, V. V.; Patil, M. M.; Navale, S. C.; Ravi, V. A Coprecipitation Technique to Prepare $ZnNb_2O_6$ Powders. *Bull. Mater. Sci.* **2005**, *28*, 205−207.
(29) Merzhanov, A. G. The Chemistry of Self-Propagating High-Temperature Synthesis. *J. Mater. Chem.* **2004**, *14*, 1779−1786.
(30) Patil, K. C.; Hegde, M. S.; Rattan, T.; Aruna, S. T. *Chemistry of Nanocrystalline Oxide Materials - Combustion Synthesis, Properties and Applications*; World Scientific Publishing Co.: NJ, 2008; p 345.
(31) Li, F.; Ran, J.; Jaroniec, M.; Qiao, S. Z. Solution Combustion Synthesis of Metal Oxide Nanomaterials for Energy Storage and Conversion. *Nanoscale* **2015**, *7*, 17590−17610.
(32) Wen, W.; Wu, J. Nanomaterials via Solution Combustion Synthesis: A Step Nearer to Controllability. *RSC Adv.* **2014**, *4*, 58090−58100.
(33) Nagaveni, K.; Hegde, M. S.; Ravishankar, N.; Subbanna, G. N.; Madras, G. Synthesis and Structure of Nanocrystalline TiO_2 with Lower Band Gap Showing High Photocatalytic Activity. *Langmuir* **2004**, *20*, 2900−2907.
(34) Sivalingam, G.; Nagaveni, K.; Hegde, M. S.; Madras, G. Photocatalytic Degradation of Various Dyes by Combustion Synthesized Nano Anatase TiO_2. *Appl. Catal., B* **2003**, *45*, 23−38.
(35) Kikkawa, S.; Hosokawa, S.; Ogawa, H. Preparation of Transparent Conductive $(ZnO)_mIn_2O_3$ Fine Powder by Gel-Combustion Reaction. *J. Am. Ceram. Soc.* **2005**, *88*, 308−311.
(36) Morales, W.; Cason, M.; Aina, O.; de Tacconi, N. R.; Rajeshwar, K. Combustion Synthesis and Characterization of Nanocrystalline WO_3. *J. Am. Chem. Soc.* **2008**, *130*, 6318−6319.
(37) Thomas, A.; Janáky, C.; Samu, G. F.; Huda, M. N.; Sarker, P.; Liu, J. P.; van Nguyen, V.; Wang, E. H.; Schug, K. A.; Rajeshwar, K. Time- and Energy-Efficient Solution Combustion Synthesis of Binary Metal Tungstate Nanoparticles with Enhanced Photocatalytic Activity. *ChemSusChem* **2015**, *8*, 1652−1663.
(38) de Tacconi, N. R.; Timmaji, H. K.; Chanmanee, W.; Huda, M. N.; Sarker, P.; Janáky, C.; Rajeshwar, K. Photocatalytic Generation of Syngas Using Combustion-Synthesized Silver Bismuth Tungstate. *ChemPhysChem* **2012**, *13*, 2945−2955.
(39) Kresse, G.; Joubert, D. From Ultrasoft Pseudopotentials to the Projector Augmented-Wave Method. *Phys. Rev. B: Condens. Matter Mater. Phys.* **1999**, *59*, 1758−1775.
(40) Blöchl, P. Projector Augmented-Wave Method. *Phys. Rev. B: Condens. Matter Mater. Phys.* **1994**, *50*, 17953−17979.
(41) Kresse, G.; Furthmüller, J. Efficient Iterative Schemes for Ab Initio Total-Energy Calculations Using a Plane-Wave Basis Set. *Phys. Rev. B: Condens. Matter Mater. Phys.* **1996**, *54*, 11169−11186.
(42) Kresse, G.; Furthmüller, J. Efficiency of Ab-Initio Total Energy Calculations for Metals and Semiconductors Using a Plane-Wave Basis Set. *Comput. Mater. Sci.* **1996**, *6*, 15−50.
(43) Perdew, J.; Chevary, J.; Vosko, S.; et al. Atoms, Molecules, Solids, and Surfaces: Applications of the Generalized Gradient Approximation for Exchange and Correlation. *Phys. Rev. B: Condens. Matter Mater. Phys.* **1992**, *46*, 6671−6687.
(44) Perdew, J. P.; Burke, K.; Ernzerhof, M. Generalized Gradient Approximation Made Simple. *Phys. Rev. Lett.* **1996**, *77*, 3865−3868.
(45) Anisimov, V.; Zaanen, J.; Andersen, O. Band Theory and Mott Insulators: Hubbard U instead of Stoner I. *Phys. Rev. B: Condens. Matter Mater. Phys.* **1991**, *44*, 943−954.
(46) Zhou, F.; Marianetti, C. A.; Cococcioni, M.; Morgan, D.; Ceder, G. Phase Separation in Li_xFePO_4 Induced by Correlation Effects. *Phys. Rev. B: Condens. Matter Mater. Phys.* **2004**, *69*, 201101−1−201101−4.
(47) Ganduglia-Pirovano, M. V.; Hofmann, A.; Sauer, J. Oxygen Vacancies in Transition Metal and Rare Earth Oxides: Current State of Understanding and Remaining Challenges. *Surf. Sci. Rep.* **2007**, *62*, 219−270.
(48) Sarker, P.; Prasher, D.; Gaillard, N.; Huda, M. N. Predicting a New Photocatalyst and Its Electronic Properties by Density Functional Theory. *J. Appl. Phys.* **2013**, *114*, 133508−1−133508−9.
(49) Sarker, P.; Al-Jassim, M. M.; Huda, M. N. Theoretical Limits on the Stability of Single-Phase Kesterite-Cu_2ZnSnS_4. *J. Appl. Phys.* **2015**, *117*, 035702−1−035702−13.
(50) Monkhorst, H.; Pack, J. Special Points for Brillouin-Zone Integrations. *Phys. Rev. B* **1976**, *13*, 5188−5192.
(51) Methfessel, M.; Paxton, A. T. High-Precision Sampling for Brillouin-Zone Integration in Metals. *Phys. Rev. B: Condens. Matter Mater. Phys.* **1989**, *40*, 3616−3621.
(52) Momma, K.; Izumi, F. VESTA: A Three-Dimensional Visualization System for Electronic and Structural Analysis. *J. Appl. Crystallogr.* **2008**, *41*, 653−658.
(53) Izumi, F.; Momma, K. Three-Dimensional Visualization in Powder Diffraction. *Solid State Phenom.* **2007**, *130*, 15−20.
(54) Press, P.; Britain, G.; Wahlstrom, E.; Marinder, B.-O.; Wahlstron, E.; Marinder, B. O. Phase Analysis Studies in the Copper-Niobium-Oxygen system. *Inorg. Nucl. Chem. Lett.* **1977**, *13*, 559−564.
(55) Langbein, H.; Woelki, G. Preparation of Copper Niobates by Thermal Decomposition of Freeze-Dried Complex Oxalate Solutions. *Thermochim. Acta* **1995**, *264*, 67−73.
(56) Kratzheller, B.; Gruehn, R. Beiträge Zum Thermischen Verhalten von Übergangsmetallniobaten III. Darstellung Und Struktur von Orthorhombischem $CuNb_2O_6$. *J. Alloys Compd.* **1992**, *183*, 75−84.
(57) Amonpattaratkit, P.; Ananta, S. Effects of Calcination Temperature on Phase Formation and Particle Size of $Zn_2Nb_{34}O_{87}$ Powder Synthesized by Solid-State Reaction. *Mater. Chem. Phys.* **2013**, *139*, 478−482.
(58) Prasatkhetragarn, A.; Ketsuwan, P.; Ananta, S.; Yimnirun, R. Effects of Vibro-Milling Time on Phase Formation and Particle Size of $Zn_3Nb_2O_8$ Nanopowders. *Mater. Lett.* **2010**, *64*, 1113−1116.
(59) Joshi, U. A.; Palasyuk, A. M.; Maggard, P. A. Photoelectrochemical Investigation and Electronic Structure of a p-Type $CuNbO_3$ Photocathode. *J. Phys. Chem. C* **2011**, *115*, 13534−13539.
(60) Joshi, U. A.; Maggard, P. A. $CuNb_3O_8$: A p-Type Semiconducting Metal Oxide Photoelectrode. *J. Phys. Chem. Lett.* **2012**, *3*, 1577−1581.
(61) Choi, J.; King, N.; Maggard, P. A. Metastable Cu(I)-Niobate Semiconductor with a Low-Temperature, Nanoparticle-Mediated Synthesis. *ACS Nano* **2013**, *7*, 1699−1708.
(62) King, N.; Sahoo, P. P.; Fuoco, L.; Stuart, S.; Dougherty, D.; Liu, Y.; Maggard, P. A. Copper Deficiency in the P-Type Semiconductor $Cu_{1-x}Nb_3O_8$. *Chem. Mater.* **2014**, *26*, 2095−2104.
(63) Xu, D.; Yang, H.; Li, L.; Zhou, Q.; Yuan, H.; Cui, T. Optical Properties of $ZnNb_2O_6$ Single Crystals Prepared via the Optical Floating Zone Technology. *Cryst. Res. Technol.* **2014**, *49*, 502−506.
(64) Pittman, R. M.; Bell, A. T. Raman Studies of the Structure of Nb_2O_5/TiO_2. *J. Phys. Chem.* **1993**, *97*, 12178−12185.
(65) Xie, S.; Iglesia, E.; Bell, A. T. Effects of Temperature on the Raman Spectra and Dispersed Oxides. *J. Phys. Chem. B* **2001**, *105*, 5144−5152.
(66) Varma, M. R.; Reshmi, C. P.; Lekshmi, P. N. Sinterability and Dielectric Properties of $ZnNb_2O_6$ − Glass Ceramic Composites. In *Advances in Ceramics - Synthesis and Characterization, Processing and Specific Applications*; Sikalidis, C., Ed.; Intech, 2011.
(67) Murphy, A. Band-Gap Determination from Diffuse Reflectance Measurements of Semiconductor Films, and Application to Photoelectrochemical Water-Splitting. *Sol. Energy Mater. Sol. Cells* **2007**, *91*, 1326−1337.
(68) Wu, W.; Liang, S.; Ding, Z.; Zheng, H.; Wu, L. A New Approach to the Preparation of Microcrystalline $ZnNb_2O_6$ Photocatalysts via a Water-Soluble Niobium-Citrate-Peroxo Compound. *Solid State Sci.* **2011**, *13*, 2019−2023.
(69) Zhou, Y.; Qiu, Z.; Lü, M.; Ma, Q.; Zhang, A.; Zhou, G.; Zhang, H.; Yang, Z. Photoluminescence Characteristics of Pure and Dye-Doped $ZnNb_2O_6$ Nanoparticles Prepared by a Combustion Method. *J. Phys. Chem. C* **2007**, *111*, 10190−10193.
(70) Rajeshwar, K. in. *Electron Transfer in Chemistry*; Balzani, V., Ed.; Wiley-VCH: Weinheim, 2001.

DOI: 10.1021/acs.jpcc.5b12738
J. Phys. Chem. C XXXX, XXX, XXX−XXX

(71) Song, X.-M.; Wu, J.-M.; Tang, M.-Z.; Qi, B.; Yan, M. Enhanced Photoelectrochemical Response of a Composite Titania Thin Film with Single-Crystalline Rutile Nanorods Embedded in Anatase Aggregates. *J. Phys. Chem. C* **2008**, *112*, 19484−19492.
(72) Li, J.; Wu, N. Semiconductor-Based Photocatalysts and Photoelectrochemical Cells for Solar Fuel Generation: A Review. *Catal. Sci. Technol.* **2015**, *5*, 1360−1384.
(73) de Brito, J. F.; Araujo, A. R.; Rajeshwar, K.; Zanoni, M. V. B. Photoelectrochemical Reduction of CO_2 on Cu/Cu_2O Films: Product Distribution and pH Effects. *Chem. Eng. J.* **2015**, *264*, 302−309.
(74) Homayoni, H.; Chanmanee, W.; de Tacconi, N. R.; Dennis, B. H.; Rajeshwar, K. Continuous Flow Photoelectrochemical Reactor for Solar Conversion of Carbon Dioxide to Alcohols. *J. Electrochem. Soc.* **2015**, *162*, E115−E122.

DOI: 10.1021/acs.jpcc.5b12738
J. Phys. Chem. C XXXX, XXX, XXX−XXX